High Efficiency Solar Power Generation with Improved Discontinuous Pulse Width Modulation (DPWM) Overmodulation Algorithms

Lan Li [1], Hao Wang [1], Xiangping Chen [2,3,]*[ID], Abid Ali Shah Bukhari [4][ID], Wenping Cao [4,]*[ID], Lun Chai [1] and Bing Li [1]

[1] College of Electrical and Power Engineering, Taiyuan University of Technology, Shanxi 030024, China; lilan@tyut.edu.cn (L.L.); wanghaom93@163.com (H.W.); chailun_tyut@126.com (L.C.); biang1221@163.com (B.L.)

[2] Electrical Engineering School, Guizhou University, Guiyang 550025, China

[3] Faculty of Engineering, Cardiff University, Cardiff CF24 3AA, UK

[4] School of Engineering and Applied Science, Aston University, Birmingham B4 7ET, UK; bukhars2@aston.ac.uk

* Correspondence: ee.xpchen@gzu.edu.cn (X.C.); w.p.cao@aston.ac.uk (W.C.)

check for updates

Abstract: The efficiency of a photovoltaic (PV) system strongly depends on the transformation process from solar energy to electricity, where maximum power point tracking (MPPT) is widely regarded as a promising technology to harvest solar energy in the first step. Furthermore, inverters are an essential part of solar power generation systems. Their performance dictates the power yield, system costs and reliable operation. This paper proposes a novel control technology combining discontinuous pulse width modulation (DPWM) and overmodulation technology to better utilize direct current (DC) electrical power and to reduce the switching losses in the electronic power devices in conversion. In order to optimize the performance of the PV inverter, the overmodulation region is refined from conventional two-level space vector pulse width modulation (SVPWM) control technology. Then, the turn-on and turn-off times of the switching devices in different modulation areas are deduced analytically. A new DPWM algorithm is proposed to achieve the full region control. An experimental platform based on a digital signal processing (DSP) controller is developed for validation purposes, after maximum power is achieved via a DC/DC converter under MPPT operation. Experimental results on a PV system show that the DPWM control algorithm lowers the harmonic distortion of the output voltage and current, as well as the switching losses. Moreover, better utilization of the DC-link voltage also improves the PV inverter performance. The developed algorithm may also be applied to other applications utilizing grid-tie power inverters.

Keywords: DPWM; MPPT; photovoltaic power system

1. Introduction

Currently, there is great concern about global warming due to the rapid depletion of fossil fuels [1]. Thus, the utilization of renewable energy has received increasing attention in industry and research communities. Solar energy is one of the most promising renewable energy sources in the world, and photovoltaic (PV) power generation systems are a growing area for research and development [2].

Conventionally, the efficiency of direct-coupled PV systems could be very low due to the high dependence on the irradiance and temperature conditions. This can be overcome by continuously tracking the maximum power point (MPP) of the system at varied conditions of irradiance and temperature [3–5]. This method is known as maximum power point tracking (MPPT). In order to

realize MPPT, DC/DC converters are commonly used in the PV power system. Moreover, the PV modules are usually connected in series to raise the output direct current (DC) voltage and, in parallel, to increase the output power. However, this will lead to a multi-peak effect, which poses a challenge to maintain the equal terminal voltage across PV modules.

On the other hand, inverters are a key component in solar photovoltaic systems, and their performance determines the power yield, system costs and reliable operation [6–8]. Most PV inverters adopt a two-level control technique based on the space vector pulse width modulation (SVPWM). The multi-peak effect potentially increases the switching losses in the power switching devices [9–12]. In order to reduce this effect, a synchronous pulse width modulation (PWM) method is often utilized in cascaded inverters [13]. When the DC voltage is low, an overmodulation control mode is adopted for the two inverters. Therefore, a T-type three-level overmodulation strategy is developed [14–16]. By doing so, PV inverters can still achieve maximum power point tracking (MPPT) which can prolong the running time of PV inverters and improve the output power. However, these technologies increase the complexity and the cost of photovoltaic power generation systems, as well as the switching losses and total harmonic distortion (THD) of the PV systems [17–20].

In this paper, a new discontinuous pulse width modulation (DPWM) scheme is proposed to achieve optimal control of PV inverters along with MPPT in a boost DC/DC converter. It combines DPWM and overmodulation to reduce device conducting periods, based on two-level SVPWM control technology [21]. As a result, the device power losses are reduced effectively. Moreover, the overmodulation segment control method can also reduce the harmonic distortion of the output voltage and improve the DC-link voltage utilization. Thereby, the overall system efficiency will be increased.

The contents are organized as follows: An equivalent circuit of a PV power system under an MPPT scheme is presented in Section 2, followed by the introduction of a DPWM overmodulation algorithm in Section 3. Section 4 demonstrates both simulation and experimental results in detail. The key findings are summarized in Section 5.

2. Equivalent Circuit of a PV Power System

Figure 1 shows the structure of a typical photovoltaic system. The MPPT control of PV panels is achieved by a DC/DC converter, which can also maintain the voltage stability of the DC bus. The PV inverter (DC/AC converter) can achieve the active/reactive power control.
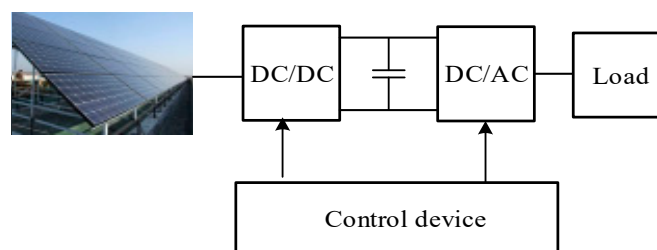

Figure 1. Structure of the photovoltaic (PV) power.

2.1. Perturbation and Observation (P&O) MPPT Algorithm

Conventionally, MPPT is embedded in a converter to determine the duty cycle that maximizes the PV power yield [22]. A perturbation and observation method (P&O) is used to find the maximum power point [23] by altering the array terminal voltage and then comparing the PV output power with its previous value. If the power increases while voltage increases, the PV array is operating in the correct direction; otherwise, the operational point should be adjusted to its the opposite direction [24,25]. The main advantage of P&O lies in its simplicity. This method shows its effectiveness, provided that solar irradiation does not change very quickly. As shown in Figure 2, there are four operational points,

A, B, C and D. From point A to point B, the PV power increases while the voltage of point B is higher than that of point A. Therefore, the next perturbation voltage keeps increasing, or vice versa. If the operation starts from point C to D, PV power decreases while the voltage of point C is higher than the voltage of point D. The next operation should be changed to the opposite direction. Therefore, the next perturbation reduces the voltage so as to redirect the trajectory towards the maximum power point. Accordingly, four scenarios are summarized in Table 1.
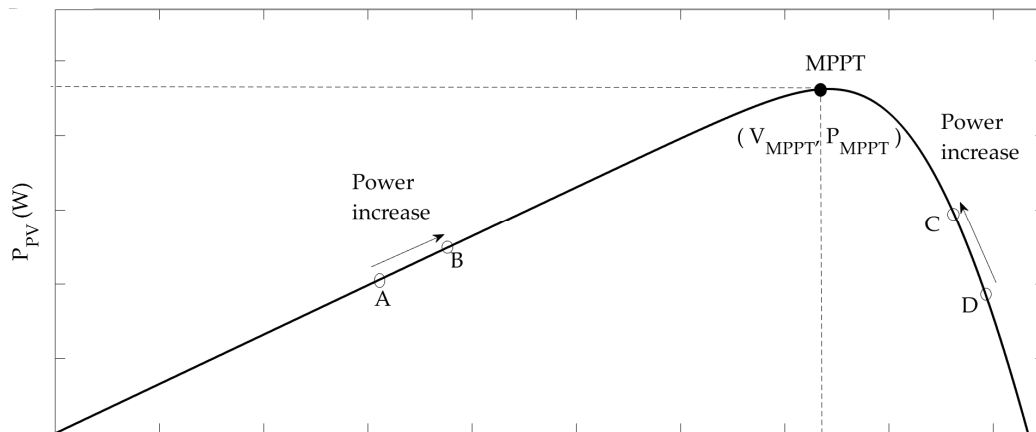

Figure 2. Maximum power point tracking (MPPT) from different trajectories.

Table 1. Trajectory analysis with perturbation and observation (P&O) MPPT.

No.	Scenario	Example Route	Action
1	$P_{current} > P_{previous}$ & $V_{current} > V_{previous}$	A → B	Increase voltage
2	$P_{current} > P_{previous}$ & $V_{current} < V_{previous}$	D → C	Decrease voltage
3	$P_{current} < P_{previous}$ & $V_{current} > V_{previous}$	C → D	Decrease voltage
4	$P_{current} < P_{previous}$ & $V_{current} < V_{previous}$	B → A	Increase voltage

A boost DC/DC converter is adopted to adjust the terminal voltage by regulating the duty ratio *D*. It will therefore incur the change of the equivalent power output which in turn realizes the maximum power output of a PV array. A flowchart of the P&O method is shown in Figure 3.
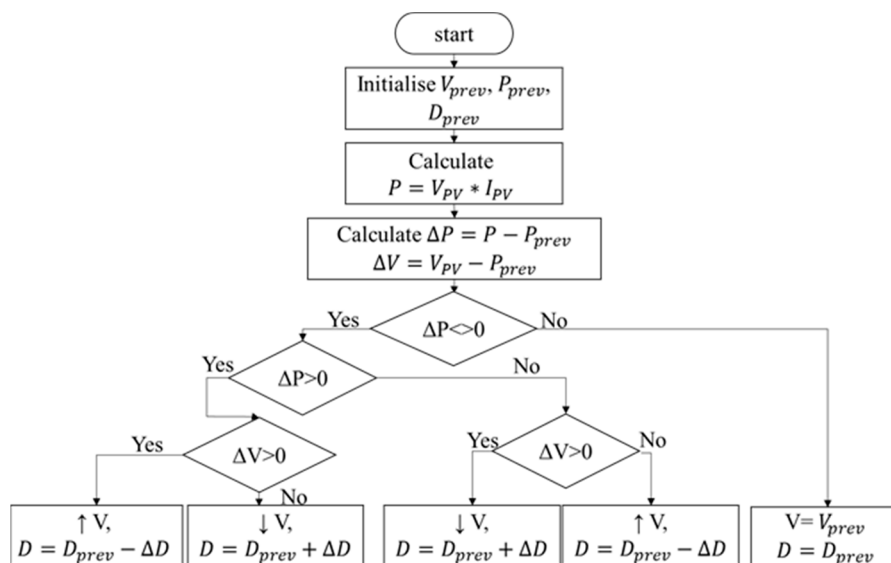

Figure 3. Flowchart of the P&O method for MPPT.

2.2. A Boost DC-DC Converter and the Equivalent Circuit

In this study, a boost converter is adopted to operate the voltage via changing D. A boost converter is expected to connect with the output of PV arrays to produce the equivalent output voltage equal to the voltage V_{mpp} at the maximum power point, with equivalent resistance equal to R_{mpp} with the current I_{mpp} over the output circuit, as shown in Figure 4. Selecting a proper DC-DC converter with reasonable circuit parameters is essential.
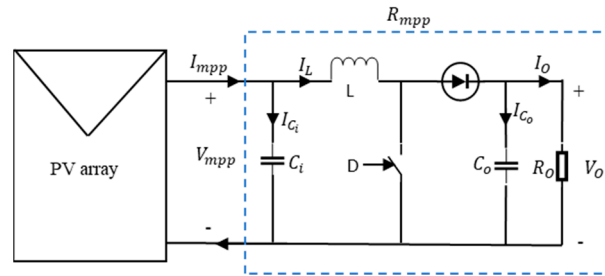

Figure 4. Equivalent circuit including a PV array and a boost DC-DC converter.

To design a boost converter for a PV system, key elements in the selection include the inductance of an inductor L', the capacitance of an input capacitor C_i, the input resistance R_{mpp}, capacitance of an input capacitor C_i, and the load resistance R_O. The purpose of this boost converter is to realize the equivalent circuit resistance to R_{mpp}. Therefore, the maximum output power under the current condition can be produced via this boost converter from a PV array.

The maximum power point resistance R_{mpp} is calculated based on the maximum power point voltage V_{mpp} and the maximum power point current I_{mpp} by using a simple calculation in Equation (1). R_O can be calculated by Equation (2). The duty ratio D can be derived from Equation (3). Assuming there is no power loss in circuit, an energy balance equation can be established (Equation (4)).

$$R_{mpp} = \frac{V_{mpp}}{I_{mpp}} \tag{1}$$

$$R_O = \frac{R_{mpp}}{(1-D)^2} \tag{2}$$

$$\text{Or} \qquad D = 1 - \sqrt{\frac{R_{mpp}}{R_O}} \tag{3}$$

$$p_{mpp} = \frac{V_{mpp}^2}{R_{mpp}} = \frac{V_O^2}{R_O} \tag{4}$$

$$\text{Or} \qquad \frac{V_{mpp}^2}{V_O^2} = \frac{R_{mpp}}{R_O} \tag{5}$$

Equation (5) presents the relationship between resistance and voltage. The output voltage is calculated from Equation (5) to Equation (6).

$$V_O = V_{mpp} \sqrt{\frac{R_O}{R_{mpp}}} \tag{6}$$

The inductance can be estimated by many methods [26,27]. A general calculation is given by Equation (7).

$$L' = \frac{V_{mpp} \cdot D}{I_{mpp} \cdot \gamma_{IL} \cdot f} \tag{7}$$

where f and γ_{IL} refer to the switching frequency and the inductor current ripple factor.

Input capacitor C_i can be calculated according to Equation (8).

$$C_i = \frac{D}{8 \cdot L \cdot \gamma_{V mpp} \cdot f^2} \tag{8}$$

Output capacitor C_O can be calculated according to Equation (9) [28].

$$C_O = \frac{D}{R_O \cdot \gamma_{VO} \cdot f} \tag{9}$$

where the current ripple factor γ_{IL} and the voltage ripple factors $\gamma_{V mpp}$, γ_{VO} are refined within 5%.

2.3. Division of the Overmodulation Area

Figure 5 presents the main circuit topology of the three-phase grid-tie inverter, where U_d is the DC-link voltage, i_a, i_b, and i_c are the inverter output currents, L is the filter inductance, and R is the filter inductance equivalent series resistance, respectively.
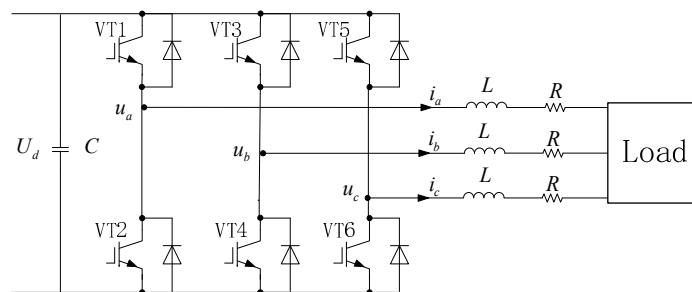

Figure 5. Topology of the three-phase grid-tie inverter.

In the inverter, the on-state of the upper arm switches and the off-state of the lower arm switches are defined as "1"; otherwise, they are "0". Therefore, the three bridge arms of the inverter have eight switch states, corresponding to eight basic voltage space vectors: $u_0(000)$, $u_1(100)$, $u_2(110)$, $u_3(010)$, $u_4(011)$, $u_5(001)$, $u_6(101)$ and $u_7(111)$. The SVPWM modulation voltage vector and the sector distribution of the PV inverter are demonstrated in Figure 6. The amplitude of $u_1 \sim u_6$ is $\frac{2}{3}U_d$, and the phase angles of $u_1 \sim u_6$ differ by 60°.
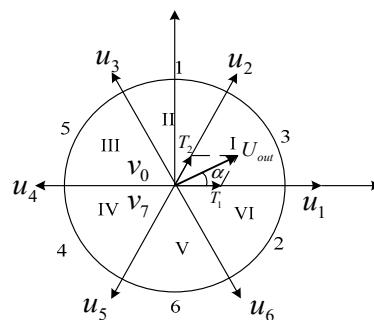

Figure 6. Space voltage vectors and sector distribution.

According to the volt-second balance principle:

$$U_{out} \cdot T_s = u_1 \cdot T_1 + u_2 \cdot T_2 \tag{10}$$

where U_{out} is the given output voltage vector, T_1 is the action time for u_1, T_2 is the action time for u_2, and T_s is the switching period.

The output space rotating vector with a constant rotating speed and a constant amplitude is achieved by the vector addition of adjacent vectors. The output range is in the inscribed circle of the regular hexagon constituted by the vectors $u_1 \sim u_6$, which are also known as the linear modulation areas. The maximum amplitude of the output phase voltage is given by:

$$u_{m\_line} = \frac{2 \cdot U_d}{3} \cdot \cos 30° = \frac{U_d}{\sqrt{3}} \tag{11}$$

If the PV inverter is controlled by the six-step wave mode outside of the linear modulation area, the amplitude of the phase voltage can be obtained [29].

$$u_{m\_max} = \frac{2 \cdot U_d}{\pi} \tag{12}$$

The region from outside the linear modulation area to the six-step maximum output voltage area is called the overmodulation area. The modulation coefficient m is defined as:

$$m = \frac{\pi \cdot U_{out}}{2 \cdot U_d} \tag{13}$$

There are three different regions as per the modulation coefficient. In the linear modulation area, $m < 0.907$; in the overmodulation area I, $0.907 < m < 0.952$; in the overmodulation area II, $0.952 < m < 1$. Figure 7 shows the trajectory of the synthesized voltage vector in the overmodulation areas. The simplified formulas for overmodulation areas I and II are given by [30–33].

$$\alpha_r = \frac{\pi}{6} - \arccos\left(\frac{U_d}{\sqrt{3} \cdot U_{out}}\right) \tag{14}$$

$$\begin{cases} \alpha_h = 6.40 \cdot m - 6.09 & (0.952 \le m < 0.9800) \\ \alpha_h = 11.57 \cdot m - 11.34 & (0.9800 \le m < 0.9975) \\ \alpha_h = 48.96 \cdot m - 48.43 & (0.9975 \le m < 1) \end{cases} \tag{15}$$

Take sector I for example. In overmodulation area I, the rotational speed of the output voltage vector remains constant and the amplitude is limited by the hexagon. The vertex of the trajectory follows the thick solid line of ABCD. In overmodulation area II, the rotation speed of the output voltage vector changes and the amplitude is limited. When $\alpha < \alpha_h$, the output voltage vector is u_1. When $\alpha_h \le \alpha < \frac{\pi}{3} - \alpha_h$, the trajectory of the output voltage vector is the BC solid line. When $\alpha \ge \frac{\pi}{3} - \alpha_h$, the output voltage vector is u_2. When $\alpha_h = \frac{\pi}{6}$, the output voltage vector traces at the vertex of the regular hexagon, and the modulation coefficient is the maximum ($m = 1$). The remaining sectors are the same.
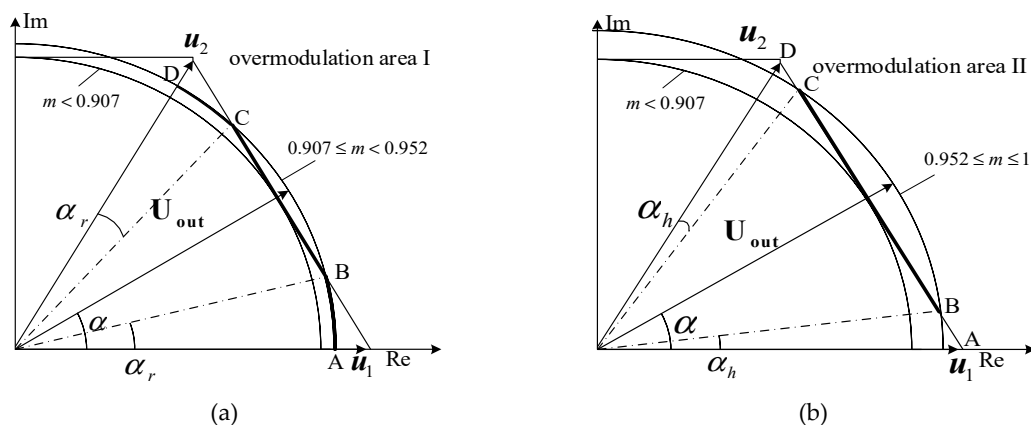

Figure 7. Synthesized voltage vector locus. (**a**) Overmodulation area I; (**b**) Overmodulation area II.

2.4. Full Modulation Region Voltage Vector

The key to controlling the voltage vector in the full modulation area is to determine the action time of the voltage vector according to the modulation coefficient m.

Take sector I for example again: U_{out} is synthesized by two basic voltage space vectors $u_1(100)$ and $u_2(110)$ and it is known that $u_1 = \frac{2}{3}U_d$, $u_2 = \frac{2}{3}U_d \cdot e^{j\frac{\pi}{3}}$. According to the sine theorem:

$$\frac{U_{out}}{\sin\frac{2\pi}{3}} = \frac{u_1 \cdot \frac{T_1}{T_s}}{\sin\left(\frac{\pi}{3} - \alpha\right)} = \frac{u_2 \cdot \frac{T_2}{T_s}}{\sin(\alpha)} \tag{16}$$

The action time T_1 and T_2 can be further calculated. When $T_1 + T_2 < T_s$, the zero vector $u_0(000)$ or $u_7(111)$ is used to fill the remaining time T_0.

(1) SVPWM linear modulation area ($m < 0.907$)

It can be obtained from Equation (16):

$$\begin{cases} T_1 = \sqrt{3} \cdot T_s \cdot \frac{U_{out}}{U_d} \cdot \sin\left(\frac{\pi}{3} - \alpha\right) \\ T_2 = \sqrt{3} \cdot T_s \cdot \frac{U_{out}}{U_d} \cdot \sin(\alpha) \\ T_0 = T_s - T_1 - T_2 \end{cases} \tag{17}$$

(2) Overmodulation area I ($0.907 \le m < 0.952$)

(i) When $0 \le \alpha \le \alpha_\gamma$ or $\frac{\pi}{3} - \alpha_\gamma \le \alpha \le \frac{\pi}{3}$, T_1, T_2 and T_0 are calculated in the same way as Equation (17).

(ii) When $\alpha_\gamma \le \alpha < \frac{\pi}{3} - \alpha_\gamma$,

$$\begin{cases} T_1 = T_s \cdot \frac{\sin\left(\frac{\pi}{3} - \alpha\right)}{\sin\left(\frac{\pi}{3} + \alpha\right)} \\ T_2 = T_s \cdot \frac{\sin(\alpha)}{\sin\left(\frac{\pi}{3} + \alpha\right)} \\ T_0 = 0 \end{cases} \tag{18}$$

(3) Overmodulation area II ($0.952 \le m < 1$)

(i) When $0 \le \alpha < \alpha_h$,

$$T_1 = T_s, \ T_2 = 0, \ T_0 = 0 \tag{19}$$

(ii) When $\alpha_h \le \alpha < \frac{\pi}{3} - \alpha_h$,

$$\gamma = \frac{\pi}{6} \cdot \frac{(\alpha - \alpha_h)}{\left(\frac{\pi}{6} - \alpha_h\right)}$$

$$\begin{cases} T_1 = T_s \cdot \frac{\sin\left(\frac{\pi}{3} - \gamma\right)}{\sin\left(\frac{\pi}{3} + \gamma\right)} \\ T_2 = T_s \cdot \frac{\sin\gamma}{\sin\left(\frac{\pi}{3} + \gamma\right)} \\ T_0 = 0 \end{cases} \tag{20}$$

(iii) When $\frac{\pi}{3} - \alpha_h \le \alpha < \frac{\pi}{3}$,

$$T_1 = 0, \ T_2 = T_s, \ T_0 = 0 \tag{21}$$

3. DPWM Overmodulation Algorithm

In traditional SVPWM modulation algorithms, A, B, and C from the given voltage vector U_{out} are calculated from the $\alpha - \beta$ coordinate plane.

$$\begin{cases} A = U_\beta \\ B = U_\alpha \cdot \sin 60° - U_\beta \cdot \cos 60° \\ C = -U_\alpha \cdot \sin 60° - U_\beta \cdot \cos 60° \end{cases} \tag{22}$$

where U_α and U_β are the α, β components of U_{out} in the $\alpha - \beta$ coordinate plane, respectively. S is defined as:

$$S = \text{sign}(A) + 2 \cdot \text{sign}(B) + 4 \cdot \text{sign}(C) \tag{23}$$

Thus, the relationship between sectors N and S can be obtained, as shown in Table 2.

Table 2. Relationship between S and N.

S	1	2	3	4	5	6
Sector N	II	VI	I	IV	III	V

As for the DPWM scheme, the switches are controlled only by the zero vector u_0 or u_7 in a triangular carrier cycle, as shown in Figure 8. u_7 is selected in the 60° range centred around the basic vectors u_1, u_3 and u_5, while u_0 is selected in other sectors. The DPWM sector number and its action conditions are tabulated in Table 3. There are twelve 30° sectors in the DPWM, as compared to six sectors in conventional SVPWM.
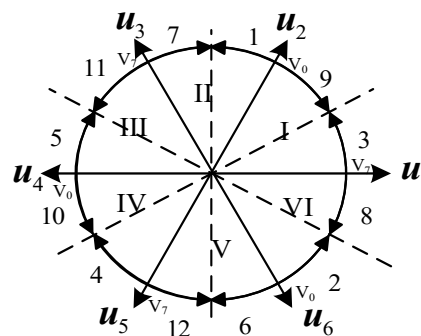

Figure 8. The sector distribution of the discontinuous width pulse modulation (DPWM).

Table 3. DPWM sector number and its action conditions.

Action condition	Sector N	S for the 30°	Sector
$\frac{U_\beta}{U_\alpha} < \tan\left(\frac{\pi}{6}\right)$	I	3 (True)	9 (False)
	IV	10 (True)	4 (False)
$U_\alpha > 0$	II	1 (True)	7 (False)
	V	6 (True)	12 (False)
$\frac{U_\beta}{U_\alpha} < -\tan\left(\frac{\pi}{6}\right)$	III	11 (True)	5 (False)
	VI	2 (True)	8 (False)

As for the DPWM modulation, the power devices switch four times in one sector because only u_0 or u_7 is used as the zero vector in one sector. Meanwhile, for the SVPWM modulation, the power devices switch six times in one sector because the vectors u_0 and u_7 are simultaneously applied (each action time is $T_0/2$).

Therefore, the switching frequency of the power devices in the DPWM modulation is reduced by one-third compared to the SVPWM modulation, and the switching sequence of the first sector is shown in Figure 9. According to the literature [34], the switching losses of the inverter power device include turn-on loss P_{on} and turn-off loss P_{off}:

$$P_{on} = \frac{1}{8} \cdot U_d \cdot t_{rN} \cdot \frac{I_{CM}^2}{I_{CN}} \cdot f_s \tag{24}$$

$$P_{off} = U_d \cdot I_{CM} \cdot t_{fN} \cdot f_s \cdot \left(\frac{1}{3\pi} + \frac{1}{24} \cdot \frac{I_{CM}}{I_{CN}} \right) \tag{25}$$

where t_{rN} and t_{fN} are the turn-on time and turn-off time, respectively; f_s is the switching frequency of power devices; I_{CN} is the forward current of IGBT; I_{CM} is the amplitude of the sinusoidal current.

Switching losses are proportional to f_s according to Equations (26) and (27), so the switching losses of the DPWM modulation can be reduced by one-third compared to the switching losses of the SVPWM modulation.
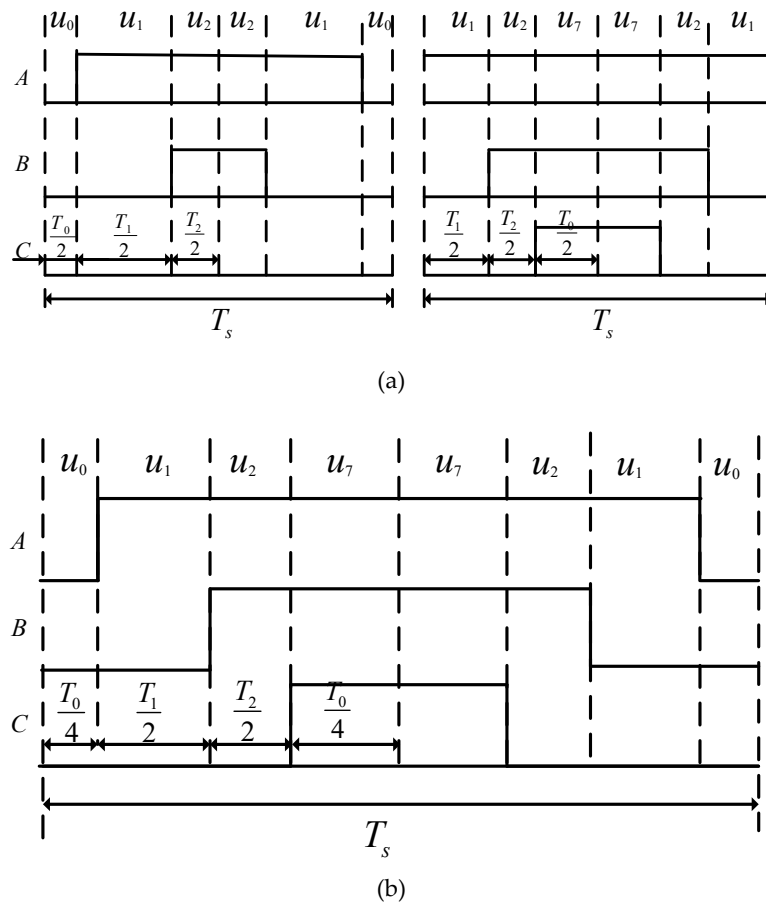

(a)

(b)

Figure 9. Switching sequences. (**a**) DPWM; (**b**) SVPWM.

4. Simulation and Experimental Validation of the Proposed Scheme

A PV inverter experimental test rig based on digital signal processing (DSP) is developed to verify the DPWM control algorithm as Figure 10a shown. DSP takes a high-performance 32-bit fixed-point TMS320F2812 as the controller (clock frequency 150 MHz, working voltage 3.3 V, Texas Instruments Incorporated, TX, USA); its chip contains 128 K 16-bit FLASH, 16-way 12-bit A/D conversion, two event managers and so on. Experimental tests are carried out by five photovoltaic panels (as shown in Figure 10b) in series under an ambient temperature of 25 °C and a daylight illuminance of 1000 W/m^2; the parameters of a single photovoltaic module are presented in Table 4. The output voltage range of the DC/DC converter (5 kW) is 100-400 V. The power module model of the DC/AC converter (2 kW) is PM30RSF060 (as shown in Figure 10c), and its maximum switching frequency is 20 kHz.

Before the proposed system is validated by the experimental tests, an MPPT algorithm with the associated equivalent circuit is simulated.

Table 4. Photovoltaic module parameters.

Open-Circuit Voltage (V)	Short-Circuit Current (A)	Max Voltage (V)	Max Current (A)	Max Power (W)
45.2	5.36	37.1	5.11	190

(a)
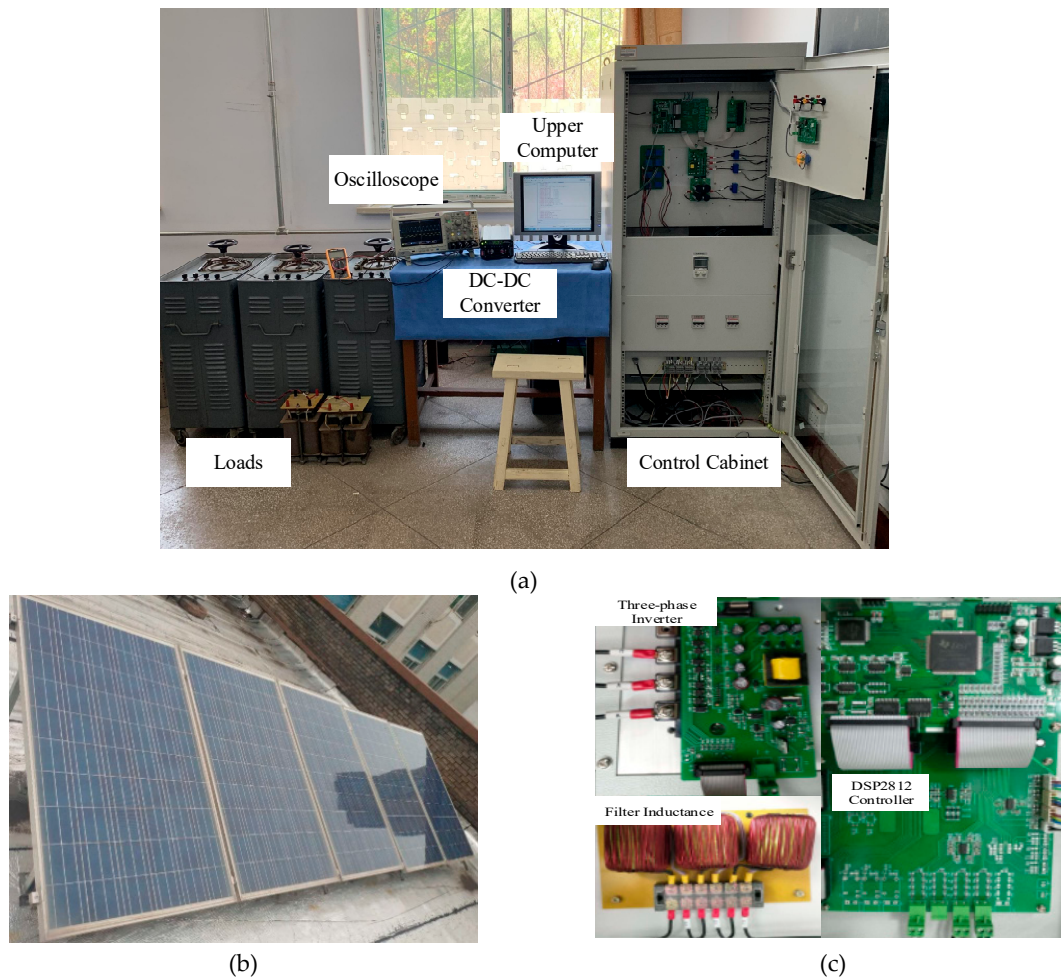

(b)

(c)

Figure 10. Experimental system. (**a**) Test rig; (**b**) Photovoltaic modules; (**c**) DC/AC converter.

4.1. Simulation Results of Different Varied Solar Irradiations

In a PV power system, the weather conditions, such as cloudy, rainy, dust, etc., will influence the power conversion. In most applications in this field, solar irradiation is considered as one of the most important factors in power generation, where weather variation will be mostly reflected in solar irradiation. We therefore test the PV power system performance as the solar irradiation varies. A series of waveforms in Figure 11 provides the auto-tracking process when the MPPT algorithm works with the DC/DC converter. Through the DC/DC converter, the output DC voltage of photovoltaic modules is kept at 140 V while the duty ratio D is 0.735 in the reference condition. In order to validate the performance of a DC/DC converter with the MPPT algorithm, varied solar irradiations are applied to the PV array. The performance is shown in Figure 11a–d.

As Figure 11a–d show, the current, the voltage and the power of the PV panel spontaneously follow the rapid variation of the solar irradiation. The proposed PV power system reaches the target of maximal utilisation of solar energy with limited oscillation, which in turn validates the excellent performance of the MPPT scheme applied in this investigation.
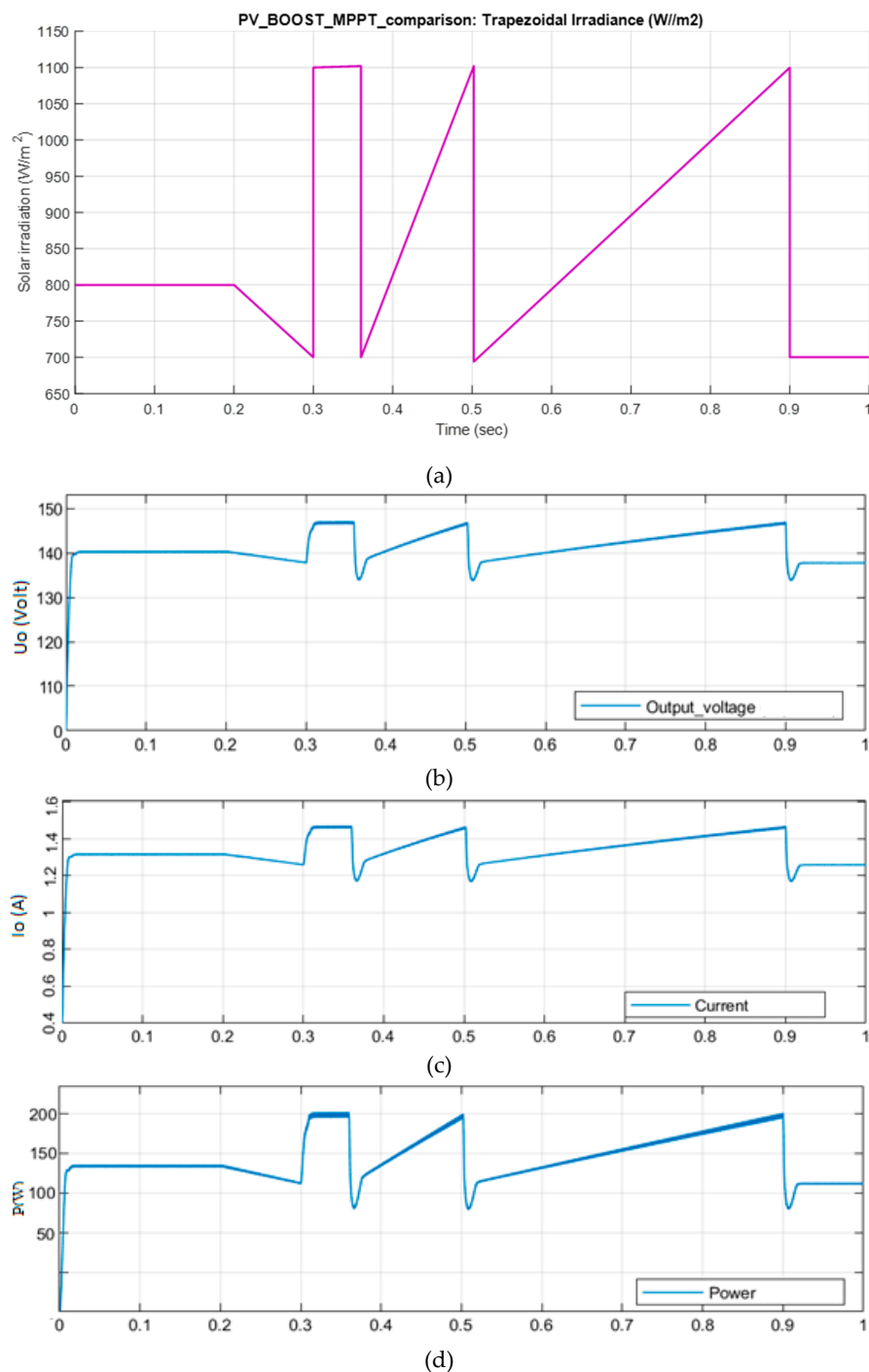
(a)

(b)

(c)

(d)

Figure 11. The performance of the DC/DC converter with varied solar irradiation. (**a**) Varied solar irradiation; (**b**) the output voltage at maximum power point (MPP); (**c**) the output current at MPP; (**d**) the output power at MPP.

4.2. DC/AC under the DPWM scheme

The DC/AC converter runs with a three-phase symmetrical resistive load ($R_L = 40\ \Omega$, $L_L = 10$ mH). The switching period is selected as $T_s = 0.0002$ s. The test waveforms are collected by the Tektronix oscilloscope TDS2024 (Test equipment Solutions Ltd, Berkshire, UK).

The control algorithm is designed to implement the proposed DPWM scheme. The flow chart of the DPWM algorithm can be obtained according to Equations (17)-(21), as shown in Figure 12.
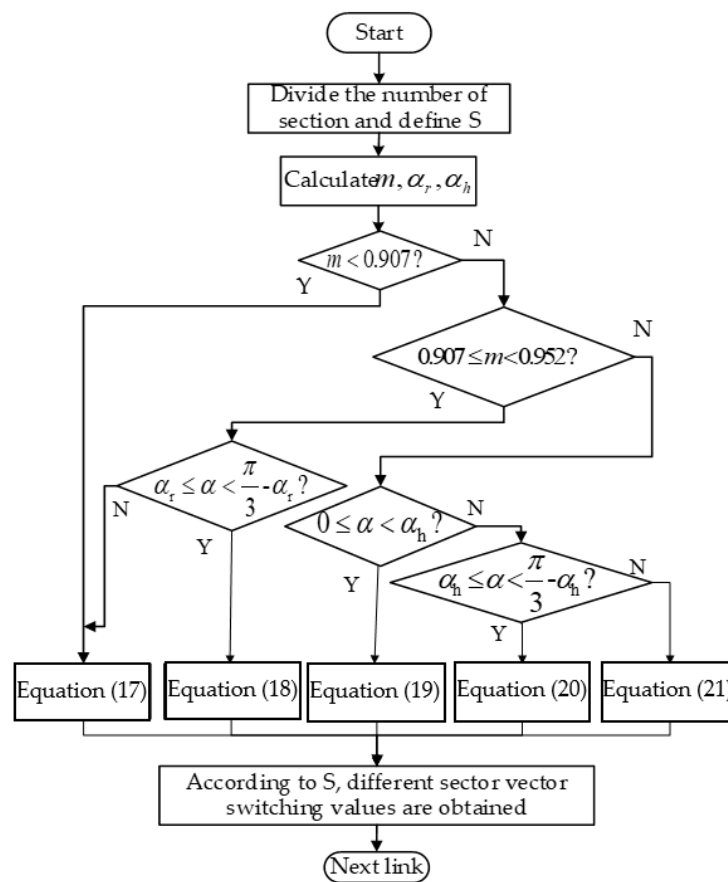
Figure 12. Flowchart of the proposed DPWM regions algorithm.

The transformation sequence of the DPWM overmodulation sector is shown in Figure 13.
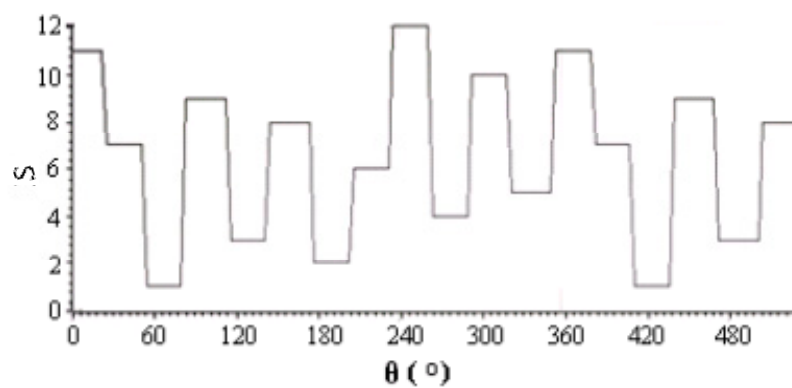

Figure 13. Sector transformation sequence.

The SVPWM modulation waveform in the linear modulation area and the DPWM modulation waveform with different modulation coefficients are shown in Figure 14.
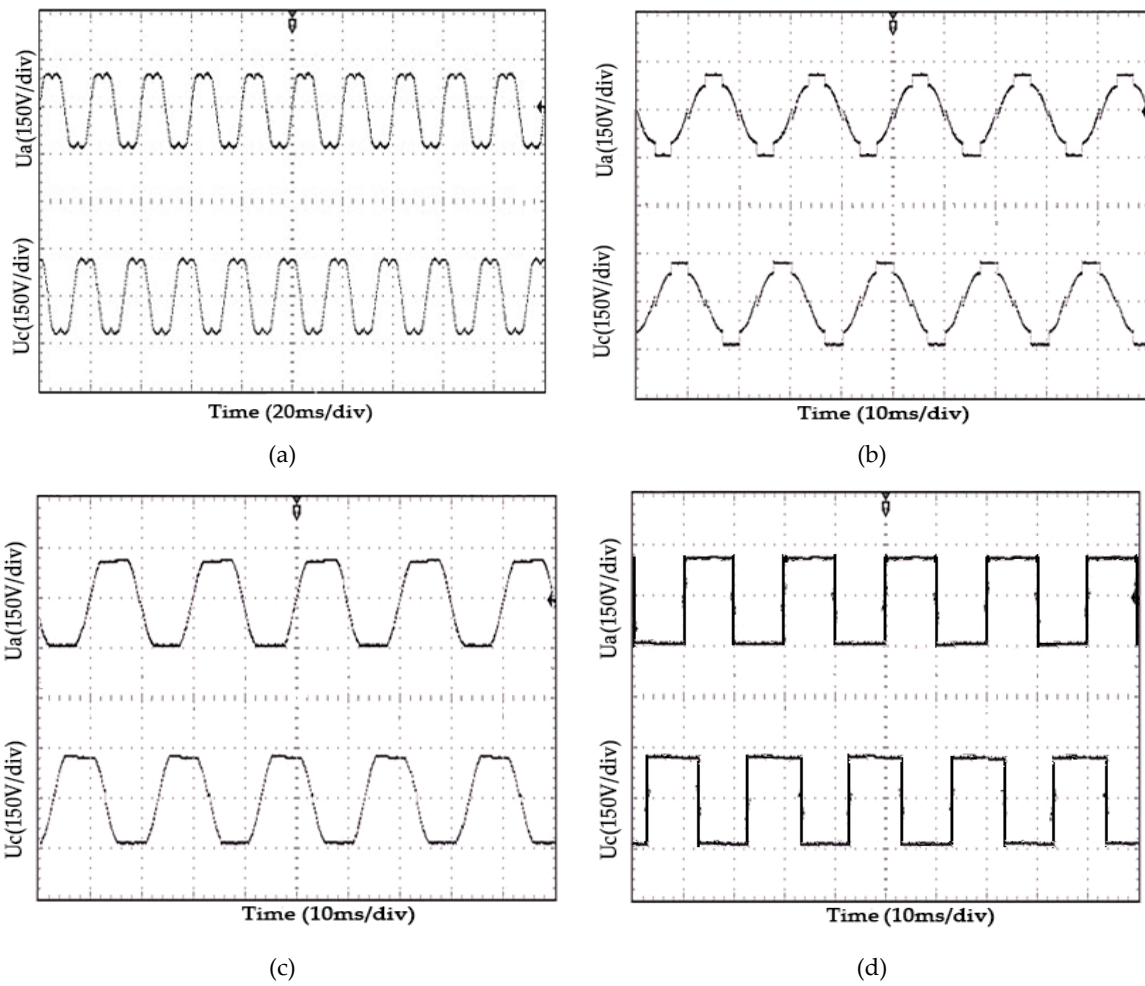
(a)

(b)

(c)

(d)

Figure 14. Modulation waveforms under different modulation schemes. (**a**) Space vector pulse width modulation (SVPWM); (**b**) DPWM (m = 0.778); (**c**) DPWM (m = 0.916); (**d**) DPWM (m = 1).

It can be seen from the figures that as the modulation coefficient increases, the peak of the DPWM modulation wave is gradually flattened and finally operates in the square wave operation state, thereby achieving linear control of the inverter output fundamental voltage over the entire modulation range.

When the modulation coefficient m = 0.92, the output pulse waveforms of TMS320F2812 under different strategies are shown in Figure 15. The waveforms of the output phase voltage and current are presented in Figure 16 and the spectral analysis results of the current are shown in Figure 17.
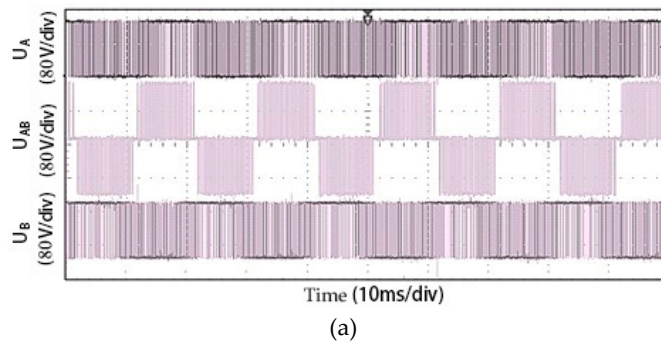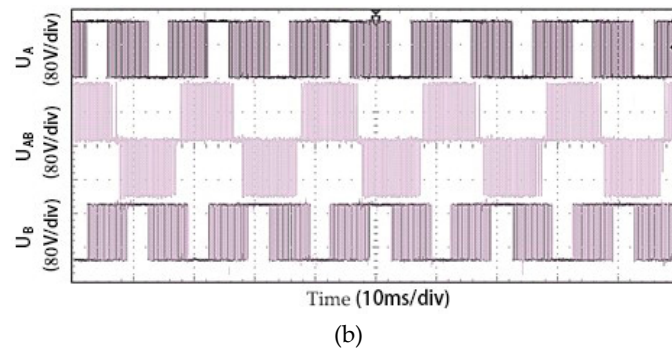

(a)

Figure 15. *Cont*.

(b)

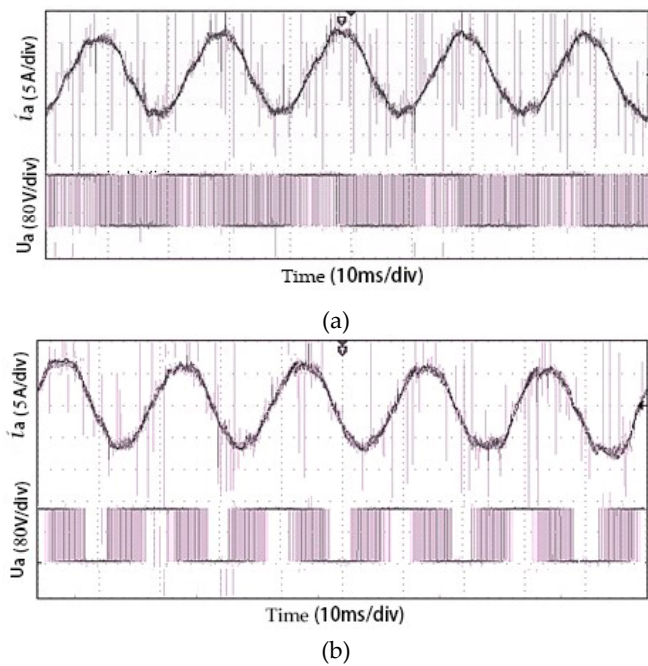**Figure 15.** Pulse waveforms under different modulation schemes. (**a**) SVPWM; (**b**) DPWM.

(a)

(b)

Figure 16. Output voltage and current waveforms. (**a**) SVPWM; (**b**) DPWM.

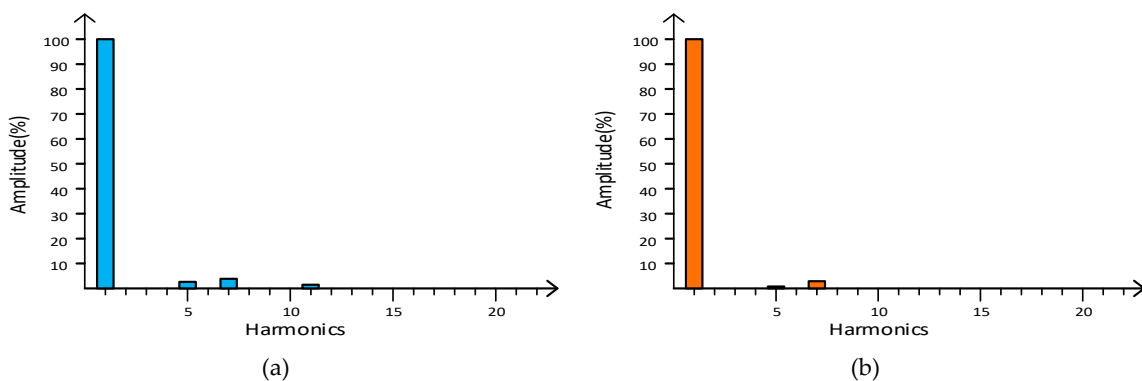(a)　　　　　　　　　　　　　　　　　　(b)

Figure 17. Spectral analysis results of the current. (**a**) SVPWM; (**b**) DPWM.

From Figures 15–17, it can be seen that the upper and lower arms are not operated in the one-third period under the proposed strategy. Compared with the switching control pulse of conventional SVPWM with the same carrier frequency, the switching time is reduced by one-third. The switching

losses can be effectively reduced so as to increase the efficiency. The harmonic contents of the load current measured by the spectrum analyzer are presented in Figure 17 and Table 5.

Table 5. Harmonic contents in the load current.

Harmonics	SVPWM	DPWM
5th	3.55%	0.93%
7th	4.84%	3.68%
11th	1.61%	0
THD	6.58%	4.40%

Clearly, the amplitude of the 5th, 7th and 11th harmonics under the DPWM modulation strategy are lower than that of the SVPWM modulation strategy. The THD of the conventional SVPWM modulation strategy is 6.58%, while that of the DPWM overmodulation strategy is reduced to 4.4%. The current waveforms of the proposed DPWM algorithm are close to sinusoidal, and it appears to have a higher utilization ratio of the DC voltage than the SVPWM. In turn, this leads to reduced switching losses and improved THD.

5. Conclusions

This paper has proposed a high-efficiency PV power generation system by combining an MPPT algorithm and a new control technology evolving from DPWM and overmodulation. It can realize the modulation of a full area on the basis of traditional SVPWMs. A DC/DC converter with an inverter simulation model and an experimental test rig are developed to justify the proposed method. The main contributions of this work are:

(i) A P&O MPPT algorithm is applied to a boost DC/DC converter so as to effectively harvest solar energy and transform to DC electricity;

(ii) A novel control technology is proposed, combining discontinuous pulse width modulation (DPWM) and overmodulation technology to better utilize the DC-link voltage.

(iii) It has been shown by measurements that through implementing this algorithm, the switching losses in the power electronic devices are reduced.

(iv) The test results have confirmed that the DPWM overmodulation algorithm can effectively reduce harmonic distortion of the three-phase output voltage and current. It has also improved the conversion efficiency of photovoltaic systems.

(v) The proposed technology is simple to implement in practical PV inverters as there are no alterations to existing hardware design. It may also be applied to other grid-tie inverters to improve their performance.

Author Contributions: In this article, L.L. and W.C. conceived and designed the system; H.W., L.C. and B.L. performed the experiments; A.A.S.B. and X.C. built the simulation models; X.C. and L.L. analyzed data and wrote the paper.

Conflicts of Interest: The authors declare no conflict of interest.

Nomenclature

α	Angle between the output voltage vector and the horizontal axis
α_γ	Angle between the intersection of the output voltage vector and the hexagon boundary, and the vertex of hexagon
α_h	Control angle to determine how long the output voltage vector stays at the vertex of hexagon
γ_{IL}	Current ripple factor of the inductor
γ_{VO}	Voltage ripple factor of the inductor

C_i,	Capacitance of the input capacitor in DC/DC converter
C_o,	Capacitance of the output capacitor in DC/DC converter
D	Duty ratio of DC/DC converter
f	Switching frequency of a DC/DC converter
i_a, i_b, i_c	Inverter output currents
I_{mpp}	Equivalent output current at maximum power point
L	Filter inductance
L_L	Symmetrical load inductance
L'	Inductance of a DC/DC converter
m	Modulation coefficient
N	Sector
p_{mpp}	Maximum power of a PV module
R	Filter inductance
R_L	Symmetrical load resistance
R_{mpp}	Equivalent resistance at maximum power point
R_O	Load resistance of the DC/DC converter
S	Sector number
T_1, T_2, T_0	Action time of adjacent fundamental voltage vectors and zero vector
T_s	Switching period
$u_0 \sim u_7$	Basic voltage space vectors
U_α, U_β	Two components of the output voltage vector in the $\alpha - \beta$ coordinates
U_d	DC-link voltage
u_m	Amplitude of the phase voltage
u_{m_max}	Maximum phase voltage in linear modulation area
U_{out}	Output voltage
V_{mpp}	Equivalent output voltage at maximum power point
V_O	Load voltage of the DC/DC converter
t_{rN}	Turn-on time
t_{fN}	Turn-off time
f_s	Switching frequency of power devices
I_{CN}	Forward current of IGBT
I_{CM}	Amplitude of the sinusoidal current

References

1. Bukhari, S.A.A.S.; Cao, W.P.; Soomro, T.A.; Guanhao, D. Future of microgrids with distributed generation and electric vehicles. In *Development and Integration of Microgrids*; Cao, W.P., Yang, J., Eds.; InTech: Rijeka, Croatia, 2017.
2. Aly, M.; Ahmed, E.M.; Shoyama, M. Modulation Method for Improving Reliability of Multilevel T-type Inverter in PV Systems. *IEEE J. Emerg. Sel. Top. Power Electron.* **2019**. [CrossRef]
3. Gosumbonggot, J.; Fujita, G. Global Maximum Power Point Tracking under Shading Condition and Hotspot Detection Algorithms for Photovoltaic Systems. *Energies* **2019**, *12*, 225. [CrossRef]
4. Baimel, D.; Tapuchi, S.; Levron, Y.; Belikov, J. Improved Fractional Open Circuit Voltage MPPT Methods for PV Systems. *Electronics* **2019**, *8*, 321. [CrossRef]
5. Afzal Awan, M.M.; Mahmood, T. A Novel Ten Check Maximum Power Point Tracking Algorithm for a Standalone Solar Photovoltaic System. *Electronics* **2018**, *7*, 327. [CrossRef]
6. Boobalan, S.; Dhanasekaran, R. Hybrid topology of asymmetric cascaded multilevel inverter with renewable energy sources. In Proceedings of the 2014 International Conference on Advanced Communication Control and Computing Technologies (ICACCCT), Ramanathapuram, India, 8–10 May 2014; pp. 1046–1051.
7. Ali, W.H.; Cofie, P.; Fuller, J.H.; Lokesh, S.; Kolawole, E.S. Performance and efficiency simulation study of a smart-grid connected photovoltaic system. *Energy Power Eng.* **2017**, *9*, 71. [CrossRef]
8. Djokic, S.; Langella, R.; Meyer, J.; Stiegler, R.; Testa, A.; Xu, X. On evaluation of power electronic devices efficiency for nonsinusoidal voltage supply and different operating power. *IEEE Trans. Instrum. Meas.* **2017**, *66*, 2216–2224. [CrossRef]

9. Zhang, X.; Li, J.; Zhao, W.; Tao, L. Review of high efficiency photovoltaic inverter. *Chin. J. Power Sources* **2016**, *4*, 931–934.

10. Wilkinson, S.; Gilligan, C. *PV Inverter Service Plans & Extended Warranties Report—2013*; HIS Technology: London, UK, 2013.

11. Suresh, K.; Prasad, M.V. Performance and evaluation of new multilevel inverter topology. *Int. J. Adv. Eng. Technol.* **2012**, *2*, 485–494.

12. Zhu, X. Three level and efficiency of photovoltaic Inverter. *Electr. Age* **2016**, *8*, 46–47.

13. Griva, G.; Oleschuk, V. Synchronous operation of dual-inverter-based photovoltaic system with low DC-voltages. In Proceedings of the 2010 International Conference on Electrical Machines (ICEM), Rome, Italy, 6–8 September 2010; pp. 1–6.

14. Park, Y.; Sul, S.K.; Hong, K.N. Overmodulation strategy for current control in photovoltaic inverter. *IEEE Trans. Ind. Appl.* **2016**, *1*, 322–331. [CrossRef]

15. Chen, W.; Sun, H.; Gu, X.; Xia, C. Synchronized space-vector PWM for three-level VSI with lower harmonic distortion and switching frequency. *IEEE Trans. Power Electron.* **2016**, *31*, 6428–6441. [CrossRef]

16. Beig, A.; Kanukollu, S.; Hosani, K.; Dekka, A. Space-vector-based synchronized three-level discontinuous PWM for medium-voltage high-power VSI. *IEEE Trans. Ind. Electron.* **2014**, *61*, 3891–3901. [CrossRef]

17. Mathew, J.; Mathew, K.; Azeez, N.B.; Rajeevan, P.P.; Gopakumar, K. A hybrid multilevel inverter system based on dodecagonal space vectors for medium voltage IM drives. *IEEE Trans. Power Electron.* **2013**, *28*, 3723–3732. [CrossRef]

18. Carrasco, G.; Silva, C.A. Space vector PWM method for five-phase two-level VSI with minimum harmonic injection in the overmodulation region. *IEEE Trans. Ind. Electron.* **2013**, *5*, 2042–2053. [CrossRef]

19. Holmes, D.; Lipo, T. *Pulse Width Modulation for Power Converters: Principles and Practice*; Wiley IEEE Press: Piscataway, NJ, USA, 2003.

20. Elmelegi, A.; Aly, M.; Ahmed, E.M. Developing Phase-Shift PWM-Based Distributed MPPT Technique for Photovoltaic Systems. In Proceedings of the 2019 International Conference on Innovative Trends in Computer Engineering (ITCE), Aswan, Egypt, 2–4 February 2019; pp. 492–497.

21. Faranda, R.; Sonia, L. Energy comparison of MPPT techniques for PV Systems. *WSEAS Trans. Power Syst.* **2008**, *3*, 446–455.

22. Espi, J.M.; Castello, J. A Novel Fast MPPT Strategy for High Efficiency PV Battery Chargers. *Energies* **2019**, *12*, 1152. [CrossRef]

23. Tan, B.; Ke, X.; Tang, D.; Yin, S. Improved Perturb and Observation Method Based on Support Vector Regression. *Energies* **2019**, *12*, 1151. [CrossRef]

24. Narendiran, S. Grid tie inverter and mppt—A review. In Proceedings of the IEEE 2013 International Conference on Power and Computing Technologies (ICCPCT), Nagercoil, India, 20–21 March 2013.

25. Mohan, N.; Undeland, T.M.; Robbins, W.P. *Power Electronics: Converters, Applications, and Design*; John, Wiley & Sons: Hoboken, NJ, USA, 2003.

26. Razman, A.; Tan, C.W. Design of boost converter based on maximum power point resistance for photovoltaic applications. *Sol. Energy* **2018**, *160*, 322–335.

27. Femia, N.; Petrone, G.; Spagnuolo, G.; Vitelli, M. Optimization of Perturb and Observe Maximum Power Point Tracking Method. *IEEE Trans. Power Electron.* **2005**, *20*, 963–973. [CrossRef]

28. Wu, X.; Liu, W.; Ruan, Y.; Zhang, L. SVPWM over-modulation algorithm and its application in two-level Inverter. *Electr. Mach. Control* **2015**, *1*, 76–81.

29. Wu, D.; Xia, X.; Zhang, Z.; Li, C. A SVPWM overmodulation method based on three-phase bridge arm coordinates. *Trans. China Electrotech. Soc.* **2015**, *1*, 150–158.

30. Zhou, X.W.; Liu, W.G.; Lang, B.H. Study on generalized discontinuous PWM algorithm and harmonic. *Small Spec. Electr. Mach.* **2007**, *11*, 5–7.

31. Jia, L.; Li, H.M.; Liang, J. Research on switching losses of an inverter under discontinuous PWM strategies. *Mech. Electr. Eng. Mag.* **2006**, *1*, 51–53.

32. Liang, W.H.; Du, X.T.; You, L.R. Realization of expend linear modulation area and overmodulation algorithm in SVPWM. *Power Electron.* **2013**, *5*, 10–12.

33. Fan, S.L.; Zhao, J.A. Novel overmodulation method based on optimized SPWM. *Power Electron.* **2013**, *6*, 26–28.

34. Mao, P.; Xie, S.J.; Xu, Z.G. Switching transients model and loss analysis of IGBT module. *Proc. Chin. Soc. Electr. Eng.* **2010**, *15*, 40–47.